

Structural Insight of the Frailty of 2D Janus NbSeTe as an Active Photocatalyst

Xiaoyong Yang^{+, [a, b]} Amitava Banerjee^{+, *[a]} and Rajeev Ahuja^[a, c]

A new family of 2D materials, Janus MTeSe (M=Nb, Mo, or W) pristine and defective monolayers have been investigated in this work as promising catalysts for hydrogen evolution reaction (HER) based on first-principles calculations. It has been observed that these Janus monolayers are dynamically and thermodynamically stable. Hybrid exchange-correlation functional (HSE06) based electronic structures reveal Janus NbTeSe is a polarized semiconductor with an indirect bandgap of 1.478 eV with excellent optical absorption capability near infra-red region. While MoTeSe and WTeSe monolayers are direct bandgap semiconductors with a suitable bandgap of 1.859 and 1.898 eV. The carrier effective masses and mobilities in MTeSe monolayer are also calculated. Subsequently, the catalytic activity of pristine as well as defective MTeSe for HER has been

identified from the reaction coordinate based on the adsorption free energy (ΔG_H^*). It is noticed that the Nb based Janus layer has comparatively weak HER activity than its peers, group VIB transition metals, Mo, W based Janus layer. The Coulomb attraction between the hydrogen and the monolayer decreases with the increase of the inner atomic radius from Nb, Mo to W, which is one of the structural frailties of 2D Janus NbSeTe as an active photocatalyst. We have further analyzed electronic structures and charge density distributions of pristine and defective MTeSe with/without H adatom to unveil the reason of the catalytic inferiority for Nb based Janus layer over W and Mo based systems. This comparative study of Janus MTeSe monolayers with HSE06 would provide a deep understanding of Janus based HER catalyst.

1. Introduction

Hydrogen is the most well-known clean energy source to tackle the enormous ongoing global energy demand with increasing the population, owing to its highest energy per mass ratio among all chemical fuels, earth abundance, and its eco-friendly simple byproduct (water) after burning this fuel.^[1–3] Mass production of low-cost hydrogen is one of the main requirements to economically viable the potential of this fuel. Among the various energy-exchange efficient approaches, photocatalytic water splitting is one of the promising, environment-friendly, and feasible ways since it is first noticed by Fujishima and Honda in TiO₂ by using photo-electrochemical cell.^[4]

The hydrogen evolution reaction (HER) (also known as hydrogen reduction reaction) is a two-electron electrochemical

half-cell reaction, taking place at the cathode in the water-splitting processes where the protons are reduced into hydrogen gas. According to the present scenario, hydrogen produced through the water-splitting process is less than 5% of the world's hydrogen.^[5,6] For maximizing the efficiency of this hydrogen production through HER, expensive noble metal catalysts such as platinum (Pt) as well as its alloys is commonly considered to reduce the overpotential and accelerate the rate of HER. In this context, it is crucial to identify the alternative low-cost and earth-abundant catalyst, which has comparable performance to that of Pt. Among the potential catalyst materials investigated so far, such as metal oxides,^[7] metal sulfides^[8] and metal nitrides,^[9,10] transition metal carbides/nitrides (MXenes),^[11,12] the 2D transition metal dichalcogenides (TMDs) with distinctive electronic and chemical properties have been attracted intense interest as a promising alternative catalyst for HER theoretically as well as experimentally.^[13–15]

However, the catalytic activity of 2D TMDs mainly constrained by the edge sites rather than the inert basal plane, although they possess high specific surface area and high ratio of exposed surface atoms.^[16] To fully utilize the potential of TMDs catalysts, various combinations of chemically functionalized materials have been synthesized by chemical vapor deposition (CVD) method to increase the number of active sites in the basal plane. On this consequence, recently, a new family called “Janus TMDs” has been theoretically reported as well as experimentally synthesized by completely replacing the top S layer with Se atoms in MoS₂, resulting in an out-of-plane structural symmetry breaking.^[17–23] In comparison to the traditional TMDs (or randomly alloyed in TMDs), the Janus monolayers possess a highly asymmetric along the z-axis. This structural asymmetry due to the polarized chemical composi-

[a] Dr. X. Yang,⁺ Dr. A. Banerjee,⁺ Prof. R. Ahuja
Condensed Matter Theory Group, Department of Physics and Astronomy,
Uppsala University 45 75120 Uppsala (Sweden)
E-mail: amitava.banerjee@physics.uu.se

[b] Dr. X. Yang⁺
State Key Laboratory of Environment-friendly Energy Materials, National
Collaborative Innovation Center for Nuclear Waste and Environmental
Safety, Southwest University of Science and Technology 50 Mianyang
621010 (China)

[c] Prof. R. Ahuja
Applied Materials Physics, Department of Materials and Engineering Royal
Institute of Technology (KTH) 100 44 Stockholm (Sweden)

[†] These authors contributed equally to this work.

Supporting information for this article is available on the WWW under
https://doi.org/10.1002/cctc.202000540

© 2020 The Authors. Published by Wiley-VCH GmbH. This is an open access
article under the terms of the Creative Commons Attribution Non-Com-
mercial License, which permits use, distribution and reproduction in any
medium, provided the original work is properly cited and is not used for
commercial purposes.

tion imposes an intrinsic strain and electric field inside the crystal (responsible for Zeeman type spin-splitting), which is absent in pristine TMDs monolayers.^[24] Those inherent strain and electric field in Janus monolayer suddenly provide us a new strategy to tune the HER activity of TMDs catalysts.

Motivated by this, in this work, we have proposed a new Janus transition metal chalcogenide, MTeSe (M=Nb, Mo, or W) based on the corresponding parent MX₂ phase to investigate their maximal efficiency in HER. Specifically, within this selected combination of chalcogenides, a series of possible Janus TMDs structures along with their electronic, optical, and catalytic properties have been systemically studied and rigorously compared with their peers' systems by using the density functional theory (DFT) framework. It has been found that out of these three-transition metal base, Nb, Mo, W, the Janus WTeSe with Te vacancy is the most promising candidate for HER, based on the optimal hydrogen adsorption free energy (ΔG_H^*). Systematic analysis of electronic structures and charge density distributions of pristine and defective MTeSe with/without H adatom has been carried out to unveil the underlying mechanism as well as the superior catalytic activity for HER. Our present work further highlights the unique property of the Janus layers, which makes it capable of separating the electron and hole into different surfaces and enhance the photocatalytic activity.

Computational Details

In this work, the ground state properties and photocatalytic performance of Janus MTeSe (M=Nb, Mo, or W) monolayers are studied through electronic structure calculations based on DFT formalism^[25] with the plane-wave pseudopotential.^[26] To solve the Kohn-Sham equations, the Vienna *ab initio* simulation package (VASP) is used.^[25,26] The valence electrons are described by a plane wave basis set with an energy cutoff of 520 eV. The Perdew-Burke-Ernzerhof (PBE) form of the generalized gradient approximation (GGA) has been employed as the exchange-correlation functional^[27] to perform the structural relaxation. Subsequently, the electronic structure of the monolayer has been calculated by using Heyd-Scuseria-Ernzerhof (HSE) screened Coulombic hybrid density functional^[28] to overcome the self-interaction errors in LDA and GGA.^[29]

The 1T- and 2H-MTeSe (M=Nb, Mo, or W) monolayers are obtained respectively from their parental MSe₂ phases in the XY-plane by substituting the entire top-layer Se with Te atoms. A vacuum thickness of 20 Å is introduced to avoid the interaction between periodic images of the surface. The ground state geometries for 1T and 2H phases of MTeSe are obtained by fully relaxing the ion positions and cell volume in the primitive cell until the total energy is less than 1.0×10^{-8} eV and the Hellmann-Feynman force on each atom is less than 0.01 eV/Å. A $4 \times 4 \times 1$ supercell of 48 atoms is used to determine the adsorption energy of hydrogenation on the system, in which the shape of the supercell is fixed while the size and the fractional atomic coordinates are fully relaxed. Brillouin zone integration is performed using a $17 \times 17 \times 1$ Monkhorst-Pack k-point mesh,^[30] which is consciously chosen through the convergence test. Moreover, the hybrid HSE06 functional with $5 \times 5 \times 1$ k-point mesh is used for electronic structure calculations. The absence of long-range (van der Waal) interactions in GGA (PBE), which is essential in this kind of material, is incorporated by using

the Grimme dispersion correction (D3).^[31] Dynamical stability of the structure is confirmed from the phonon band structure and phonon DOS, which are computed with the finite displacement approach as implemented in the PHONOPY package.^[32] The thermal stability of Janus MTeSe at room temperature is examined by *ab initio* molecular dynamics (MD) simulation. The constant atom number, volume, and temperature (NVT) canonical ensemble is simulated by adopting the algorithm of Nosé thermostat.^[33] All the MD calculations are run for 20 ps with a time step of 1 fs in $4 \times 4 \times 1$ supercell. Charge transfer during the dehydrogenation process is identified from the Bader charge approach^[34] and charge density distribution.

Besides, the stability of Janus MTeSe monolayer is further evaluated by calculating two energy parameters, i.e., cohesive energy and enthalpy of formation. The cohesive energy is defined by the following equation,

$$E^{\text{coh}} = E(\text{MTeSe}) - N_M E(M) - N_{\text{Te}} E(\text{Te}) - N_{\text{Se}} E(\text{Se}) \quad (1)$$

Here, $E(\text{MTeSe})$ is the total energy of the optimized MTeSe monolayer, M=Nb, Mo, or W. $E(M)$, $E(\text{Te})$ and $E(\text{Se})$ represent the energies of isolated M, Te and Se atom, respectively. Correspondingly, N_M , N_{Te} and N_{Se} denote the total number of the specific atom in the system. Atomic energies are calculated by placing the atom in a 20 Å^3 vacuum and considering spin polarization explicitly. Within this definition, the more negative for the cohesive energy suggests easier to form the MTeSe monolayer with the exothermic formation process.^[35]

Analogously, the enthalpy of formation (E^{ent}) is estimated from the relaxed bulk energy of M, Te, and Se atom, respectively. The reference energies are chosen in their stable elemental structures of the hexagonal structure for Te and Se with P3₁2₁ space group (No. 152) and the face-centered cubic structure for Nb, Mo, and W atoms with Im-2m space group (No. 229), respectively. The sign definition is the same as in equation (1) for E^{coh} .

2. Results and Discussions

2.1. Structural properties of MTeSe monolayers

The atomic models of Janus MTeSe (M=Nb, Mo, or W) monolayers can be constructed from their parental TMD MX₂ (M=Nb, Mo, or W, X=Se or Te) structures. Thus Janus MTeSe monolayers also exhibit a honeycomb pattern from the top view of the lattice similar to MX₂. In detail, MTeSe monolayer is composed of three atomic layers stacked in a sequence of Se-M-Te, which possess two possible forms (1T and 2H phases), as shown in Figure 1.

Specifically, the 2H structure exhibits a hexagonal lattice with AB type atomic stacking sequence, as depicted in Figure 1(a). Correspondingly, the space group of MTeSe monolayer is changed to C_{3v} (from D_{3h} of 2H-MX₂) due to mirror symmetry breaking. Whereas, the 1T phase shows an ABC atomic stacking sequence that both sides of Te and Se atoms locate at the hollow center of the 2H hexagon lattice formed by the transition metal in Figure 1(b). Therefore, the mirror symmetry [(x,y,z)→(x,y,-z)] of pristine MTeSe has been broken owing to the different atomic radius and electronegativity of Te and Se

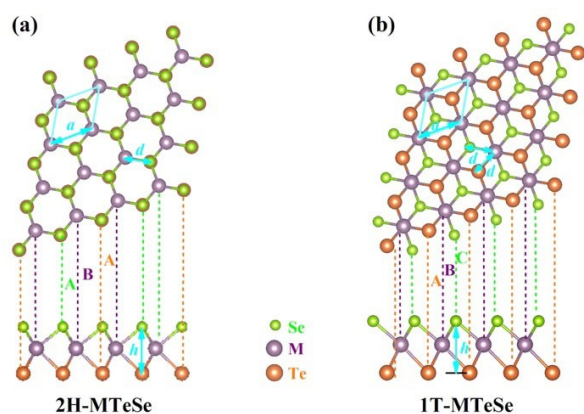


Figure 1. Top and side views of Janus MTeSe ($M=\text{Nb}$, Se , or Te) monolayer in (A) 2H and (B) 1T phase. Light green, wine, and orange balls represent Se , M , and Te atoms, respectively.

atoms, which results in inequivalent $M\text{--Te}$ and $M\text{--Se}$ bond lengths and the polar properties of MTeSe monolayers.

The optimized lattice parameters, bond lengths, sheet thicknesses and the energetic parameters of Janus MTeSe monolayers and their pristine counterpart are tabulated in Table 1. As we can verify in Table 1, the lattice parameters a , and thicknesses h of Janus MTeSe structures are between their parent structures of $M\text{Te}_2$ and $M\text{Se}_2$. Moreover, the bond lengths $d_{M\text{--Te}}$ and $d_{M\text{--Se}}$ of Janus MTeSe monolayers are also very close to those pure $M\text{Se}_2$ and $M\text{Te}_2$ structures.^[35] For example, the obtained lattice constants, bond lengths of 2H-MoTeSe are respectively 3.405 Å and 2.713 Å for $d_{M\text{--Te}}$ and 2.548 Å for $d_{M\text{--Se}}$ with a sheet thickness of 3.491 Å which are slightly shorter than those of MoTe_2 but a little larger than those of MoSe_2 . The other compositions follow the same behavior. It demonstrates that the structural parameters of Janus MTeSe monolayers are mainly governed by the chalcogen composition, and they follow the increasing of the atomic radius.

Stability of these 2D materials is one of the major concerns for practical application. Hence, this study is thoroughly investigated the structural stability along with the cohesive

energy and enthalpy of formation of 2H and 1T phases. It has been seen in Table 1 that the cohesive energies of Janus layers mostly follow the sequence of $E_{M\text{Se}_2}^{\text{coh}} < E_{2\text{H-MTeSe}}^{\text{coh}} < E_{1\text{T-MTeSe}}^{\text{coh}} < E_{M\text{Te}_2}^{\text{coh}}$, with increasing the chalcogen atomic radius. Whereas, the enthalpy of formation E^{ent} does not follow the similar trend. For example, the calculated enthalpies of formation of 2H-MoTeSe and 1T-MoTeSe are respectively -1.945 eV and -0.795 eV. So, they are not in between their parent phases, as shown in Table 1. Precisely, the lower cohesive and enthalpy of formation of 2H phase confirm that 2H-MTeSe is energetically more favorable than 1T-MTeSe. Therefore, only the catalytic performance of 2H-MTeSe is considered in the following study. Different configurations of chalcogens also affect the charge transfer. As shown in Table 1, for 2H-NbTeSe monolayer, the metallic Nb loses 1.221 e, and Te and Se atoms gain 0.480 e and 0.733 e, respectively. Whereas the Nb loses more charges of 1.226 e in 1T-NbTeSe monolayer, which implies more strong interaction among Nb, Te and Se atoms, directly resulting in the higher cohesive energy and enthalpy of formation for 1T phase. Importantly, more charge transfer to Se atom rather than Te causes the net electric field points from Te to Se atoms. Qualitatively same trends are noticed for MoTeSe and WTeSe, as illustrated in Table 1.

Consequently, the dynamic stability of the 2H-MTeSe monolayer is confirmed by the absence of any imaginary frequency in the calculated phonon dispersion (as shown in Figure S1). Thus, it could be feasible to synthesis the dynamical stable 2H-MTeSe structures with an exothermic reaction. Meanwhile, the thermal stability of 2H-MTeSe is qualitatively tested by MD simulation at room temperature. Figure S2 shows the fluctuations of ground total energies and structures after MD simulation for Janus 2H-MTeSe monolayers. One can see the total energy of each Janus MTeSe oscillation persistently occurs at a fixed value. Moreover, there is no bond-breaking and structural distortion in the final configurations of Janus monolayers. These results indicate that 2H-MTeSe monolayers could be experimentally feasible to synthesis at room temperature.

Besides, experimental studies on monolayer MoS_2 show that S vacancy concentration is important, which can shift the band edge level with respect to the redox level of water and

Table 1. Calculated lattice constants a , bond lengths $d_{M\text{--Te}/M\text{--Se}}$, sheet thicknesses h , cohesive energies E^{coh} , enthalpies of formation E^{ent} , Charge transfer ΔQ of metallic M ($M=\text{Nb}$, Mo , or W) by PBE functional.

System	a [Å]	d_{M-X} [Å]	h [Å]	E_{coh} [eV/atom]	E^{ent} [eV]	ΔQ [e]
1T-NbTeSe	3.548	2.809/2.610	3.538	−4.909	−2.567	1.226
2H-NbTeSe	3.562	2.817/2.602	3.520	−4.933	−2.640	1.221
NbTe_2 ^[35]	3.70	2.82	3.69	−4.34	−1.01	0.36
NbSe_2 ^[35]	3.48	2.62	3.37	−4.92	−1.37	0.90
1T-MoTeSe	3.345	2.764/2.537	3.623	−4.127	−0.795	0.683
2H-MoTeSe	3.405	2.713/2.548	3.491	−4.511	−1.945	0.662
MoTe_2 ^[35]	3.56	2.74	3.62	−3.97	−0.86	0.24
MoSe_2 ^[35]	3.33	2.55	3.35	−4.53	−1.21	0.76
1T-WTeSe	3.345	2.763/2.542	3.629	−4.876	−0.920	0.756
2H-WTeSe	3.401	2.718/2.552	3.509	−5.064	−1.483	0.740
WTe_2 ^[35]	3.56	2.74	3.63	−4.46	−0.66	0.19
WSe_2 ^[35]	3.32	2.55	3.36	−5.10	−1.09	0.60
2H-MoS ₂ ^[35]	3.19	2.42	3.13	−5.07	−1.42	0.90

subsequently affect the performance of the system.^[13] So, the intrinsic defects are likely to appear during the growth of Janus MTeSe monolayers. This study considered the intrinsic defect formation by evaluating the defective formation energy, which is defined as

$$E^{\text{for}} = E(V_{\text{Te/Se}}) - E(\text{MTeSe}) + \Delta\mu_{\text{Te/Se}}, \quad (\text{M} = \text{Nb, Mo, or W}). \quad (2)$$

In Eq. (2), $E(V_{\text{Te/Se}})$ is the total energy of the defective MTeSe monolayer with an isolated Te (or Se) vacancy. $\Delta\mu_{\text{Te/Se}}$ is the energy per Te (or Se) atom in its equilibrium bulk phase. The reference states are chosen as the ground state of trigonal Te and α monoclinic Se bulk phases, respectively. Here, we have considered only the charge neutral defects similar to Ref. [21]. The calculated results (as depicted in Table 2) show that the formation energy of Te vacancy is slightly lower than that of Se vacancy among this three 2H-MTeSe. It indicates that the defective formation energy of MTeSe exhibits a strong relationship with the atomic radius and electronegativity differences of chalcogen Te and Se atoms. For example, the formation energy of V_{Se} is 2.614 eV, which decreases to 1.327 eV for V_{Te} in NbTeSe monolayer. Therefore, both Te and Se vacancies in Janus MTeSe are energetically favorable at 3.125% concentration. This concentration is defined as the percentage of chalcogen atoms

moved, i.e., $\left(\frac{\text{Se (Te) Vacancy}}{\text{Se+Te}} \times 100\%\right)$. This defect concentration (3.125%) is quite reasonable with the experimentally synthesized CVD Janus structures of defect concentration of 3.8%^[17] and 5.5%^[19] and 4.9% in 2H-MoS₂.^[13]

2.2. Electronic properties

To have a better understanding of the electronic property of Janus layer with different inert transition metal plane (Nb, Mo, or W), we have calculated the band structures of all considered pristine systems with PBE (Figure S3) and screened hybrid (HSE06) functional (Figure 2) in the first Brillouin zone along with the high symmetry directions. Clearly, the band gaps calculated by HSE06 are prominently higher than those from PBE calculations. It is worth noting in Figure 2(a) that Janus

NbTeSe monolayer is a magnetic semiconductor, in accordance with its parent NbSe₂ monolayer. Since both spin-up and spin-down channels are showing indirect band gaps of 1.478 eV and 0.917 eV, which can be considered as an optimal candidate for the spintronic device. Specifically, the indirect band gap arises between the Γ_V and K_C points for the spin-up channel. Meanwhile, it appears between Γ_V and M_C points for the spin-

Table 2. Calculated formation energy E^{for} for defective MTeSe (M=Nb, Mo, or W), work function on Te (Se) side Φ_{Te} (Φ_{Se}), and potential difference between two sides of chalcogen $\Delta\Phi$.

	2H-NbTeSe Pristine	V_{Te}	V_{Se}	2H-MoTeSe Pristine	V_{Te}	V_{Se}	2H-WTeSe Pristine	V_{Te}	V_{Se}
E^{for}	–	1.327	2.614	–	2.036	3.151	–	1.981	3.244
Φ_{Te}	5.214	4.923	4.976	5.308	4.543	4.867	5.048	4.652	4.645
Φ_{Se}	5.364	5.111	5.066	5.592	5.150	5.355	5.261	5.054	5.075
$\Delta\Phi$	0.150	0.188	0.090	0.284	0.607	0.488	0.213	0.402	0.430

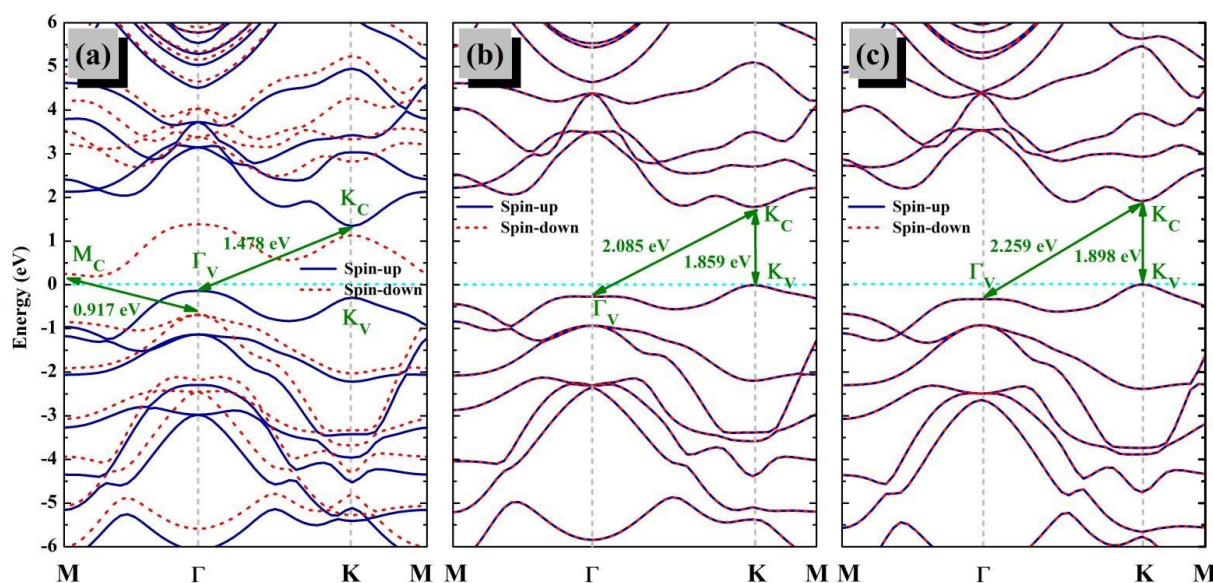


Figure 2. Calculated band structures with spin-up (blue solid lines) and spin-down for states (red dash lines) for (a) NbTeSe, (b) MoTeSe, and (c) WTeSe monolayer by HSE method, respectively. Fermi energy is set to be the zero energy.

down channel. In the case of Janus MoTeSe and WTeSe monolayers, the spin-polarized band structures in Figure 2(b) and (c) shows that both of them are nonmagnetic semiconductor with direct band gaps of 1.859 eV and 1.898 eV at the K point, respectively. Besides, there is another maximum of the valence band at Γ for MoTeSe and WTeSe monolayers, leading to indirect band gaps of 2.085 eV and 2.259 eV, respectively, which could facilitate the charge carrier transition upon photoexcitation process. Particularly, compare to their parent disulfide (MSe_2) and diselenide (MTe_2) ($M=Mo$, or W) monolayers,^[36] the band gaps of Janus MTeSe follow the same order of $MSe_2 > MTeSe > MTe_2$. Significantly, the calculated bandgaps of MTeSe ($M=Nb$, Mo , or W) are all within the visible light region, which could suggest them as potential water-splitting photocatalysts.

2.3. Effective mass and carrier mobility

The effective mass of the charge carrier could be a critical factor to characterize the HER catalyst by specifying the mobility of charge carrier and consequently the electron-hole recombination possibility. The effective masses of the electron (m_e^*) and hole (m_h^*) are calculated from the curvature of the CBM and VBM along with the high symmetry point of the hybrid functional (HSE06) band structure, by using the following equation,

$$m^* = \pm \hbar^2 \left(\frac{d^2 E_k}{dk^2} \right)^{-1}, \quad (3)$$

where k is the wave vector, and E_k is the energy of the electron that corresponds to k . The obtained values are summarized in Table 3. Specifically, according to the nearly free electron model, by fitting the spin-up and spin-down bands of Janus NbTeSe monolayer, the estimated effective masses of electrons are 0.332 m_0 and 0.751 m_0 , respectively. Correspondingly, the effective masses of holes are 0.324 m_0 and 0.739 m_0 with respect to the spin-up and spin-down states. In MoTeSe monolayer, the effective masses of electron and hole are respectively 0.646 m_0 and 0.741 m_0 , which are much larger than those of MoS_2 monolayer with 0.342 m_0 for electron and 0.428 m_0 for hole.^[37] These values are close to $\sim 0.90 m_0$ for 1T' $MoSSe$ monolayer.^[38] The actual difference between calculated values depend on the lattice constants and the approximation

used.^[39,40] In case of pristine WTeSe monolayer, the effective masses of electron and hole are sharply decreased to be 0.463 m_0 and 0.458 m_0 , respectively. As we all know that the small effective mass of the carrier could give quick response to the force of an external field, resulting in the high carrier mobility. Thus, the transport of carriers in the spin-up state is relatively faster than in the spin-down state for NbTeSe monolayer, indicating NbTeSe monolayer is a promising spin electric semiconductor. It is worth to mention that WTeSe could also have high carrier mobility due to the slightly smaller effective masses, which transfer the carriers rapidly to a favorable position during the photocatalytic. This indicates WTeSe could exhibit compelling photocatalytic property in the water splitting, which is following the predicted trend of similar structure.^[21]

Thus, carrier mobility, another vital parameter for the application of materials in photocatalysis, is evaluated by acoustic phonon scattering via intra- and intervalley deformation potential (DP) couplings at room temperature, which is calculated by DP theory as expressed below,^[41]

$$\mu = \frac{2eh^2C}{3k_B T |m^*| E_d^2} \quad (4)$$

Where m^* is the obtained effective mass of electron or hole, \hbar is Planck's constant and k is the wave vector in momentum space. k_B and T are the Boltzmann constant and temperature (300 K), respectively. $C = [\partial^2 E / \partial \delta^2] / S^0$ is the elastic modulus, in which E is the ground total energy, δ is the applied uniaxial strain, and S^0 is the area of Janus MTeSe monolayer. $E_d = \Delta E / \delta$, in which ΔE is the band-edge shift with respect to the lattice change. And the uniaxial strain is defined as $\delta = \Delta a / a_0$, where a_0 is the lattice constant of Janus MTeSe. The calculated CBM and VBM positions and relative energy of Janus MTeSe as a function of the uniaxial strain are shown in Figure S4 and S5, respectively. The elastic stiffness C is calculated to be a constant with the value of 94.552, 98.600 and 99.321 N/m for NbTeSe, MoTeSe and WTeSe monolayer, respectively. The mobility of electron and hole are about 40.771 $cm^2 V^{-1} s^{-1}$ and 116.758 $cm^2 V^{-1} s^{-1}$ for MoTeSe monolayer, respectively. As for WTeSe monolayer, the electron mobility is about 68.338 $cm^2 V^{-1} s^{-1}$ and the hole mobility is about 282.863 $cm^2 V^{-1} s^{-1}$. While, for NTeSe monolayer, the mobilities of carriers in the spin-up state are higher than these in spin-down state, as shown in Table 3. Moreover, the difference of

Table 3. Calculated effective masses (m^*), elastic modulus (C), deformation potentials (E_d) and carrier mobilities (μ) of Janus MTeSe monolayer ($M=Nb$, Mo , or W). m_0 is the free electron mass.

System	Carrier	C [N/m]	E_d [eV]	m^* / m_0	μ [$cm^2 V^{-1} s^{-1}$]
NbTeSe (Spin-up)	e	94.552	8.110	0.332	184.941
	h	94.552	4.424	0.324	652.577
NbTeSe (Spin-down)	e	94.552	9.306	0.751	27.451
	h	94.552	4.310	0.739	132.138
MoTeSe	e	98.600	9.065	0.646	40.771
	h	98.600	4.670	0.741	116.758
WTeSe	e	99.321	9.805	0.463	68.338
	h	99.321	4.872	0.458	282.863

carrier mobilities between electron and hole for WTeSe monolayer is slightly larger than that of NbTeSe and MoTeSe monolayers, which indicates the effective separation of electron-hole pairs and the small probability of recombination for photogenerated carriers, significantly improving the photocatalytic activity of WTeSe monolayer.

2.4. Optical properties

The visible light absorption ability of MTeSe (M=Nb, Mo, or W) monolayers are determined from their optical absorption spectrum, with hybrid (HSE06) functional base on the ground state electronic structures according to the method proposed by Hajdoš et al.^[42] The details of the optical response calculations are shown in the supporting formation. The calculated imaginary part of the transverse dielectric constants $\epsilon(\omega)$ and the absorption coefficients $I(\omega)$ with respect to the photon energy of pristine MTeSe are depicted in Figure S6 and Figure 3, which are polarized the in-plane (\parallel) and out-of-plane (\perp) for the systems. It can be seen that the basic nature of the imaginary parts is similar and a significant blue shift occurs upon moving from Nb, Mo to W, which is qualitatively consistent with the trend of their band gaps. Specifically, the first peak of NbTeSe monolayer emerges at 1.052 eV and 2.976 eV for the in-plane and the out-of-plane direction. While, they are appearing at 2.44 eV (5.332 eV) and 2.635 eV (5.675 eV) for the in-plane (the out-of-plane) direction of MoTeSe and WTeSe monolayer, respectively. For the optical absorption spectrum, we find that Janus MTeSe monolayers allow a broad wavelength range of optical absorption from near-infrared to ultraviolet. Specifically, it can be seen distinctly that all MTeSe monolayers exhibit better optical absorption under visible-light region of 1.65 eV to 3.26 eV, and the orders of visible light absorption coefficient is in the order of NbTeSe($1.65 \times 10^5 \text{ cm}^{-1}$) < MoTeSe($2.554 \times 10^5 \text{ cm}^{-1}$) < WTeSe($2.733 \times 10^5 \text{ cm}^{-1}$). Besides, optical spectra also show the presence of the absorption peak at a higher photon energy between 4 eV–5 eV. The strong visible and ultraviolet light absorption will provide an obvious advantage for Janus MTeSe as the ideal photocatalysts. Remarkably, NbTeSe monolayer expands its optical absorption into the ultraviolet light region with the intense peak of

$1.436 \times 10^5 \text{ cm}^{-1}$, which strongly demonstrates NbTeSe monolayer is a promising candidate to be an efficient photocatalyst in the ultraviolet light region.

Thus, we further carefully investigated the work function Φ with the help of electrostatic potential calculations in the vertical direction of the monolayer according to the equation of $\phi = V_\infty - E_f$. Here, V_∞ is the vacuum potential in the vicinity of the Janus MTeSe monolayer layer, and E_f is the corresponding Fermi energy level. The obtained values for pristine and defective Janus MTeSe monolayers are listed in Table 2. For pristine NbTeSe, MoTeSe, and WTeSe monolayers, the calculated work functions of Φ_{Te} (Φ_{Se}) are 5.214 (5.364), 5.308 (5.592), and 5.048 (5.261), respectively. To the best of our knowledge, the work function is extremely sensitive to the surface morphology and concentration of impurities, which are also tools for bandgap engineering of catalysts for HER. Here, we notice that Φ_{Te} is more sensitive to defect than that of Φ_{Se} on MTeSe surface. For an instant, the Φ_{Te} decreases by 0.291 eV, reaching to 4.923 eV when Te vacancy is introduced in NbTeSe, whereas, it changes Φ_{Se} slightly by 0.253 eV to 5.111 eV. More remarkable, the work function for the Te layer side is always lower than that for the Se layer side, indicating the surface charge polarization effect is more prominent for the Te surface than that for the Se surface. The corresponding difference of electrostatic potential $\Delta\Phi$ are also collected in Table 2.

2.5. HER activity of Janus MTeSe monolayers

The overall equation of HER at the cathode is as follows,



To understand the photocatalytic property of Janus MTeSe (M=Nb, Mo, or W) in the photocatalyst, the hydrogen adsorption energy of the reaction intermediate (H^*) is extensively explored under equilibrium condition for all the possible adsorption sites, such as on top, hollow, bridge and vacancy positions on both Te and Se surfaces of MTeSe monolayers, as shown in Figure 4. The hydrogen adsorption energies are calculated by using the following equation,

$$E^{\text{ads}} = E(\text{MTeSe} + H^*) - E(\text{MTeSe}) - 1/2 E(H_2), \quad (6)$$

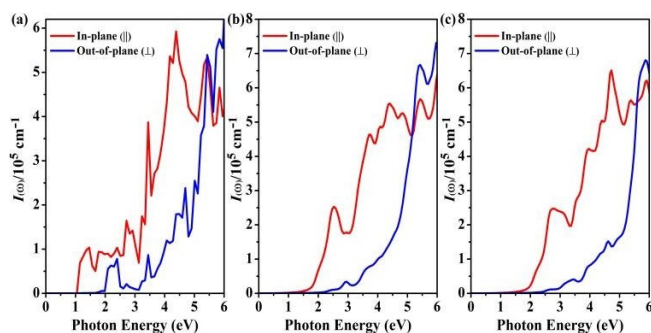


Figure 3. Calculated absorption coefficients $I(\omega)$ of Janus (a) NbTeSe, (b) MoTeSe and (c) WTeSe monolayers, respectively.

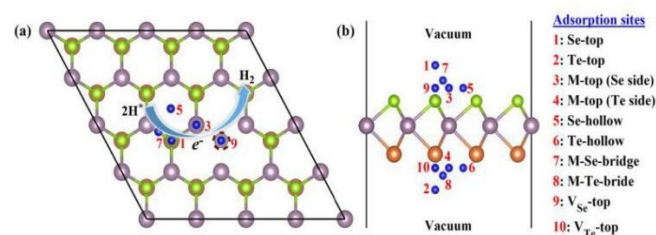


Figure 4. Adsorption of single H atom at different sites of Janus MTeSe 4×4 supercell from (a) top view and (b) side view.

where, $E(\text{MTeSe} + \text{H}^*)$ is the ground total energy of Janus MTeSe monolayer with adsorbed H atom, and $E(\text{H}_2)$ is the total energy of isolated H_2 molecule.

Corresponding adsorption free energy of the intermediate hydrogen (ΔG_{H^*}) on the catalyst surface, which is a key descriptor of the HER activity, is subsequently obtained by,^[6]

$$\Delta G_{\text{H}^*} = E^{\text{ads}} + \Delta E_{\text{ZPE}} - T\Delta S_{\text{H}} \quad (7)$$

where ΔE_{ZPE} and ΔS_{H} are respectively the difference in the zero-point energy and entropy between the hydrogen adsorbed state and gas phase. Contribution of ΔE_{ZPE} and ΔS_{H} is usually very small. Specifically, the zero-point energy of the hydrogen adsorbed state is depended mainly on the vibration frequency of H^* on different Janus layers, which is calculated from the vibrational frequency of the H atom at 0 K. The ΔS_{H} is obtained by $\Delta S_{\text{H}} \approx -\frac{1}{2}S(\text{H}_2)$, where $S(\text{H}_2) = 130.680 \pm 0.003 \text{ J} \cdot \text{K}^{-1} \cdot \text{mol}^{-1}$ ^[43] is the entropy of H_2 molecule under standard condition: 1 bar of H_2 , pH=0 and $T=300 \text{ K}$. Therefore, including ΔE_{ZPE} and ΔS_{H} corrections, the Eq. (9) for different Janus layers could be re-written as,

$$\begin{aligned} \Delta G_{\text{H}^*} &= E^{\text{ads}} + 0.269 \rightarrow \text{for NbTeSe}, \\ &= E^{\text{ads}} + 0.238 \rightarrow \text{for MoTeSe}, \\ &= E^{\text{ads}} + 0.236 \rightarrow \text{for WTeSe}, \end{aligned} \quad (8)$$

All calculated adsorption energies are presented in Table S1 (see the supporting Information). An ideal HER catalyst should have the thermoneutral condition, i.e., $\Delta G_{\text{H}^*} = 0$.

The adsorption free energies (ΔG_{H^*}) of hydrogen on MTeSe monolayers (along with the corresponding value of Pt ^[44]) with the reaction coordinate at equilibrium potential and pH=0 are depicted in Figure 5. The calculated ΔG_{H^*} for pristine NbTeSe, MoTeSe, and WTeSe monolayers are 0.222 eV, 1.789 eV, and 1.970 eV, respectively, which increases with increasing atomic radius of transition metal atoms. Whereas, the introduction of intrinsic defects largely reduces the ΔG_{H^*} for Janus MTeSe ($M=\text{Nb, Mo, or W}$) monolayers, especially the intrinsic Se vacancy. For instance, the ΔG_{H^*} value decreases to -0.037 eV for 3.125% Te vacancy but to -0.093 eV for 3.125% Se vacancy in WTeSe monolayer, which agree the previously reported results of similar Janus MSSe ($M=\text{Mo, or W}$) monolayer^[21] and traditional 2D TMDs.^[15,21] This bonding strength between H atom and MTeSe monolayer is deeply associated with the atomic radius and electronegativity differences of chalcogen Te and Se atoms. Here, it is noteworthy to mention that Janus WTeSe monolayer with 3.125% intrinsic Te vacancies is closer to the criterion of the thermoneutrality with $\Delta G_{\text{H}^*} = -0.0037 \text{ eV}$. Remarkably, it is also very close to the most expensive noble metal catalyst, Pt ,^[44] as shown in Figure 5.

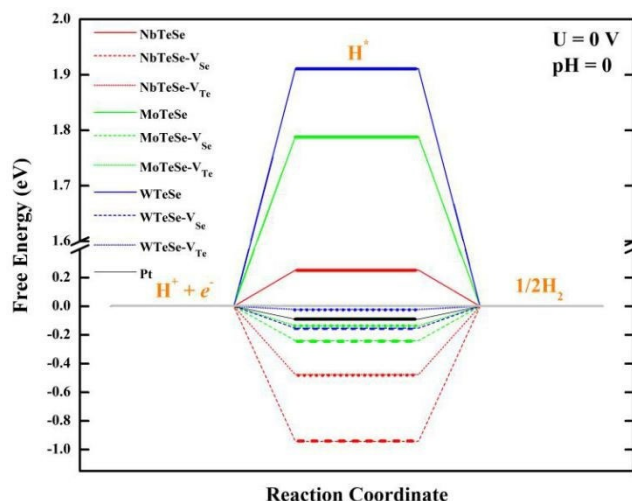


Figure 5. Adsorption Free energy diagram for hydrogen evolution reaction on pristine and defective MTeSe monolayer ($M=\text{Nb, Mo, and W}$).

Moreover, it is observed from Figure 5 that the proton transfer is solely endothermic with pristine Janus layer. While it becomes exothermic process with the introduction of intrinsic vacancy. Evidently, it is worth noting that the bonding of H atom with Janus MTeSe monolayers is markedly strengthened when Te- or Se-vacancy is introduced, which has the following tendency $\text{MTeSe-V}_{\text{Te}} > \text{MTeSe-V}_{\text{Se}} > \text{pristine MTeSe}$ ($M=\text{Nb, Mo, or W}$). This trend is in agreement with the previous theoretical results of $\text{MSSe-V}_{\text{Se}} > \text{MSeSe-V}_{\text{S}} > \text{pristine MSSe}$ ($M=\text{Mo, or W}$).^[21] In conclusion, the concentration of the intrinsic defect of Janus MTeSe could tune the chemical interaction of H with the substrate in a favorable manner such as $\Delta G_{\text{H}^*} \approx 0$.

As a second step, H_2 can be released via two possible reactions, namely Heyrovsky or Tafel reaction mechanism.^[2,3] The Heyrovsky mechanism ($\text{H}^+ + \text{H}^* + \text{e}^- \rightarrow \text{H}_2$) involves a combination of a solvated proton with one adsorbed hydride H^* from the catalyst surface to form H_2 . Another possible scheme is the Tafel reaction ($\text{H}^* + \text{H}^* \rightarrow \text{H}_2$), where two adsorbed hydride H^* on the catalyst can combine to form H_2 molecule. Given these possible mechanisms, an important issue is whether hydrogen can diffuse rapidly from one binding site to the adjacent one to form H_2 on the surface of the catalyst. To address this question, we calculate the diffusion barrier of a H atom on the MTeSe monolayer using the climbing image nudged elastic band (CI-NEB) method.^[45] The calculated migration energy barriers are 0.549 eV, 0.384 eV, and 0.464 eV for an isolated H atom diffusion on NbTeSe, MoTeSe, and WTeSe surfaces, respectively, as shown in Figure 6. It implies that the H atom could diffuse faster on MoTeSe monolayer than the other two Janus layers. This fast diffusion of H thus enables a continuous H supply around the structurally active sites of MoTeSe monolayer, where the H–H coupling and subsequent H_2 desorption occur more efficiently.

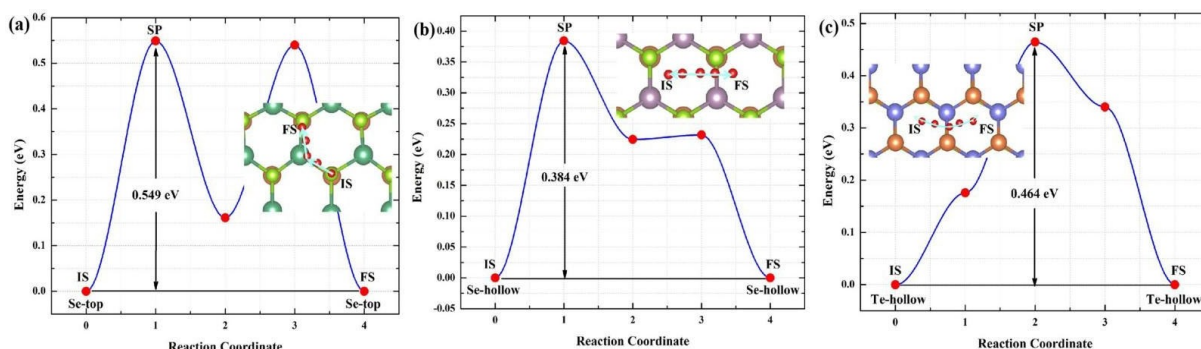


Figure 6. Minimum energy paths calculated using the CI-NEB method as a function of the liner distance along the path for a H adatom diffusion on (a) NbTeSe, (b) MoTeSe, and (c) WTeSe surfaces, respectively. The inserts shows the diffusion pathways.

2.6. Density of states and *d*-band theory

To better understand the influence of vacancy defect on the intermediate step of HER as well as the orbital contribution of band structures, we have calculated the spin-polarized total density of states (TDOS) and partial density of states (PDOS) for both pristine and defective Janus MTeSe ($M = \text{Nb, Mo, and W}$), as shown in Figure 7. In this figure we can observe that the most predominant feature is several localized energy levels at spin-up and spin-down channels below the valence band (VB) and beyond the conduction band (CB), which are mostly dominated by transition metal's *d* orbital along with a strong overlap of chalcogenide's *p* orbital, which is similar to previous studies on MX_2 .^[46] For pristine NbTeSe monolayer, the DOS for spin-up and spin-down components are different. In the case of NbTeSe monolayer with the absorbed H atom, the spin component

induces an additional electronic level in the middle of the band gap, leading to the metallic character, which is mainly dominated by Nb-4*d* band with slight hybridization between Nb-4*d* band and H-*s* orbital, as depicted in Figure 7(b). The *d*-band center is located at -3.403 eV, which is similar to the pristine NbTeSe monolayer. However, Fermi level shifts up by 0.353 eV (from -2.588 eV to -2.235 eV) after H adatom absorption on the surface of NbTeSe, leading to the shift of the *d*-band slightly away from the Fermi level, which also causes attenuation in the DOS close to the Fermi level, as shown in Figure 7(a)–(b). Interestingly, we do not observe any electronic levels inside the band gap for hydrogen-adsorbed on MoTeSe and WTeSe monolayers in Figure 7(f) and 7(j), respectively. In the defective NbTeSe monolayer, it shows the metallic nature, which is originating from the distinct spin-up states of Nb-4*d* at -2.41 eV near VBM in Figure 7(c).

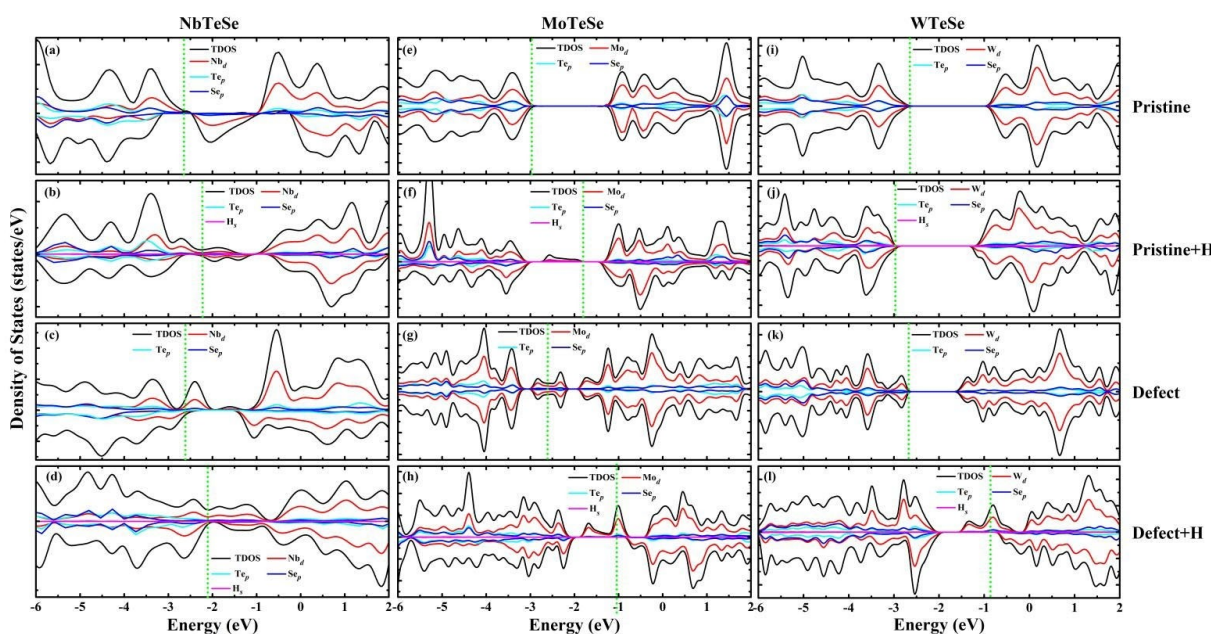


Figure 7. The calculated spin polarized total density of states (TDOS) and the projected density of states (PDOS) for (a–d) NbTeSe monolayer, (e–h) MoTeSe monolayer, and (i–l) WTeSe monolayer with or without a H adatom, respectively. The Fermi energies are denoted by green dotted lines.

Besides, the *d*-band center is slightly closer to the Fermi level compare to the pristine one in Figure 7(a), resulting in the stronger chemisorption of atomic hydrogen on the defective surface of NbTeSe monolayer. Similarly, the introduction of vacancy induces a defect peak between -2.895 eV and -2.176 eV in the DOS for MoTeSe monolayer in Figure 7(g). However, the defect levels sit within the VB (in the vicinity of the Fermi energy) for defective WTeSe monolayer in Figure 7(k). Compare to Figure 7(c), 7(g), and 7(k) for defective MTeSe monolayer, the *d*-band center locates gradually farther away from the Fermi level with increasing the atomic number of transition metal from Nb, Mo to W atom. Thus, it is not surprising that the adsorption energy of hydrogen on the surface of MTeSe becomes slowly weaker as depicted in Figure 5. Noticeably, H chemisorption on defective NbTeSe monolayer drastically changes the DOS in Figure 7(d), especially several states of spin-up and spin-down due to the contribution of hydrogen's *s* orbital, indicating half-metallic property. More importantly, only two spin-up peaks emerge between the band gap for MoTeSe and WTeSe monolayers, which are dominated respectively by Mo-4*d* and W-5*d* orbitals with minor contributions from chalcogenide's *p* orbitals in Figure 7(b) and 7(l). The sharper in-gap states in Janus monolayers with H chemisorption correspond to the flatter bands. Subsequently, the Fermi energy for the adsorption of H on substrates with Te vacancy shifts from VBM towards the defect state. Specifically, the split-off state has appeared at -1.35 eV below the Fermi level for MoTeSe monolayer and at -1.06 eV for WTeSe monolayer, which corresponds to the bonding overlap (σ) of Mo-4*d* and W-5*d* band with the H-*s* orbital, respectively. In comparison to Janus WTeSe, the position of this state is shifted slightly further down from the Fermi level in MoTeSe, which is implying the relatively stronger interaction of H-*s* state with Mo-*d* band and leading to stronger chemisorption than that with Mo atom, which could decrease the photocatalytic efficiency due to slower release H₂ gas. Besides, it confirms our aforementioned finding based on the reaction coordinate analysis that the defective MoTeSe has a more negative adsorption free energy (ΔG_{H^+}) than that of defective WTeSe in Figure 5. Meanwhile, the anti-bonding overlap (σ^*) of the metal *d* with H-*s* orbital leads to the unoccupied states which are located at 0.065 eV and

0.017 eV above the Fermi level for MoTeSe and WTeSe, respectively. The closer *d*-band center energy to Fermi level of the transition metal indicates the less filling of antibonding states, which leads to stronger bonding with an adsorbate H atom according to Nørskov's *d*-band theory.^[47,48] It is interesting to see that WTeSe–V_{Te} + H system exhibits the metallic character due to the hybridization of H-*s* and W-5*d* orbitals both below and above the Fermi energy. Therefore, as a whole, the formed bonding and anti-bonding states are responsible for having the more energetically favorable H adsorption on Janus WTeSe with Te vacancy. Since the underlying electronic structure ultimately defines the chemical interaction of H with the substrate, further analysis of band structure in Janus WTeSe monolayer can provide a deeper insight of the pronounced HER catalytic activity at Te vacancy site. The calculated band structures of pristine and defective WTeSe with and without H adatom are displayed in Figure 8. The *d* orbital-resolved projections band structures and the corresponding average projection weight with spin-up and spin-down states of MTeSe monolayer are depicted in Figure S7–9.

For the pristine + H system, the analysis of the projected bands reveals that the valence band maximum is mainly composed of out-of-plane orbital *d*_{z²} with partial in-plane orbitals of *d*_{xy} and *d*_{x²–y²} of W atoms as well as H-*s* orbital, as shown in Figure S7. For the defective WTeSe monolayer, the valence band top state is mainly dominated by *d*_{z²} orbital (17.86%) and *d*_{x²–y²} (11.18%) while the conduction band bottom states are mainly attributed by *d*_{x²–y²} and chalcogenide's *pz* orbitals, as shown in Figure S9. For the case of hydrogenated defective WTeSe monolayer, the W-5*d* orbital is splitted into: (1) one degenerated *d*_{xy} and *d*_{x²–y²} orbitals across the Fermi level with spin-up state which is slightly filled by H-*s* electron; and (2) non-occupied *d*_{z²} and *d*_{x²–y²} orbitals with spin-down state located above the Fermi level, as shown in Figure S9. The incomplete occupation of the degenerated orbitals results in a metallic-like character of the electronic structure for defective WTeSe + H system. Additionally, we have performed the Bader analysis and charge density difference between the hydrogenated and dehydrogenated WTeSe monolayer to describe the chemical bonding characteristics. It is found the H adatom gets ~ 0.22 *e* from the pristine WTeSe.

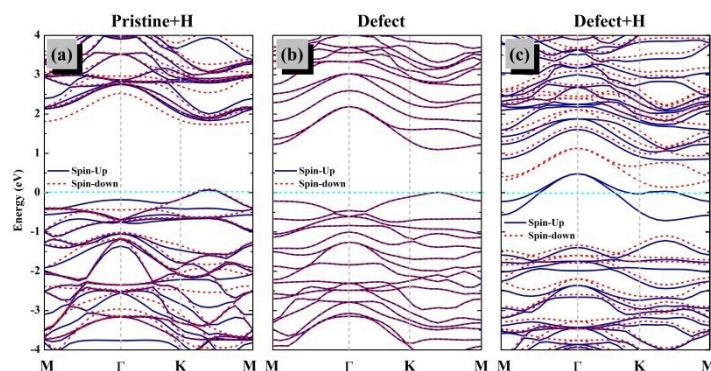


Figure 8. (a) Band structure of the pristine WTeSe with a H adatom, (b) Band structure of the defective WTeSe monolayer with the Te vacancy, and (c) Band structure of the defective WTeSe monolayer with a H adatom.

While the vacancy of Te or Se atom can provide more electrons to its nearby atoms in defective WTeSe monolayer. Thus, the adsorbed H atom gains more electrons, i.e., 0.38 e and 0.39 e from the Se and Te mono-vacant Janus WTeSe layer, respectively, which can also be reflected from the charge density difference plot (Figure S10). The more amount of charge taken by hydrogen from the monolayer in the case of defective Janus monolayer, the more stable H adsorption for the Volmer process forms, leading to decrease the H–H recombination. It is therefore conclusive that the intrinsic defects as well as unique electric field due to the Janus asymmetry play a crucial role in determining the HER activity of Janus transition-metal dichalcogenides layers, which is regarded having a great application prospect in the catalysis field.

3. Conclusions

In this work, we have performed a comprehensive study to analyze the catalytic activity for the proposed new Janus NbTeSe along with its neighbor group VI (Mo, W) monolayer based on the reaction coordinate via first-principles calculations. It is found that these 2D Janus monolayers are structurally stable and would certainly, which indicates the experimental feasibility to synthesis this Janus layer. The band structure of Janus NbTeSe exhibits a magnetic semiconductor nature with an indirect band gap of 1.478 eV, while MoTeSe and WTeSe monolayers are direct band-gap semiconductors with suitable band gap of ~ 1.85 eV. Effective mass, carrier mobility and optical spectra are also calculated to evaluate the mobility of charge carriers and visible light absorption ability. It is found that the effective masses of carriers and the difference between the effective masses of electrons and holes are both gradually decreased with increasing the atomic number from Nb, Mo to W. Moreover, all of them exhibit excellent optical absorption under visible light spectrum. Janus NbTeSe even expands its optical absorption into the near-infrared light region. The catalytic activity for HER has been identified from the reaction coordinate based on ΔG_{H^+} . It is observed that the WTeSe monolayer with Te vacancy holds the most promising as photocatalyst with -37 meV adsorption free energy. The actual influence of Te vacancy on this highly promising HER activity is thoroughly investigated by analyzing the electronic DOS and charge density distribution. Adsorption of H atom forms a stable bonding and anti-bonding states near Fermi level with Te vacancy on Janus WTeSe monolayer, which decreases the chemisorption energy. The enhanced HER catalytic activity of WTeSe monolayer over NbTeSe is attributed to the intrinsic vertical electric field with the broken mirror symmetry, which brings eccentric electronic and optical properties for photocatalysis. Our theoretical study based on the reaction coordinate, optical spectra, electronic DOS and the carrier's effective masses as well as carrier mobility, unveils the frailty of Janus NbTeSe as an active HER catalyst to split the water.

Supplementary Information

The details about calculating the optical response properties. Table for adsorption energies E^{ads} and adsorption free energies of hydrogen ΔG_{H^+} (eV) on Janus MTeSe monolayer (M=Nb, Mo, or W). Phonon dispersion and phonon density of Janus NbTeSe, MoTeSe, and WTeSe monolayers, respectively. The total energies and final configuration of MTeSe monolayer by MD simulations. Band structures with spin-up and spin-down states for Janus MTeSe monolayers. Band edge positions and total energy as a function of the uniaxial strain along x for MTeSe monolayer, respectively. Imagery part of Janus MTeSe monolayer. Main projections of the band structures and the corresponding average projections weight with spin-up and spin-down states for pristine and defective WTeSe monolayer with/without hydrogen adatom, respectively. Contour map of the charge density difference of H adsorption on pristine WTeSe monolayer, WTeSe with 3.125% Se vacancy, and WTeSe with 3.125% Te vacancy, respectively.

Acknowledgements

A.B. and R.A. acknowledge respectively the Carl Tryggers Stiftelse for Vetenskaplig Forskning (CTS: Grant 18.04) and Swedish Research Council (VR Grant 2016-06014). XY acknowledge for providing fund by National Natural Science Foundation of China (Grant No. 11705152, 11625415, and 41272050), by the Joint Fund of the National Natural Science Foundation of China and the China Academy of Engineering Physics (Grant No. U1530258), and Longshan academic talent research supporting program of Southwest University of Science and Technology (Grant No. 18LZX513 and 18LZX04). XY also want to acknowledge financial support from China Scholarship Council. We also thank Ziwei Wang for help to draw the figures. SNIC, HPC2N, and UPPMAX are acknowledged for providing computing time.

Conflict of Interest

The authors declare no conflict of interest.

Keywords: 2D monolayer • Defect • HER • Janus layer • water splitting

- [1] J. A. Turner, *Science* **2004**, *305*, 972–974.
- [2] X. Yang, A. Banerjee, R. Ahuja, *Catal. Sci. Technol.* **2019**, *9*, 4981–4989.
- [3] X. Yang, A. Banerjee, Z. Xu, Z. Wang, R. Ahuja, *J. Mater. Chem. A* **2019**, *7*, 27441–27449.
- [4] A. Fujishima, K. Honda, *Nature* **1972**, *238*, 37–38.
- [5] J. Gong, R. Luque, *Chem. Soc. Rev.* **2014**, *43*, 7466–7468.
- [6] A. Banerjee, S. Chakraborty, N. K. Jena, R. Ahuja, *Appl. Ener. Mater.* **2018**, *1*, 3571–3576.
- [7] Z. Zou, J. Ye, K. Sayama, H. Arakawa, *Nature* **2001**, *414*, 625.
- [8] B. Han, Y. H. Hu, *Energy Sci. Eng.* **2016**, *4*, 285–304.
- [9] M. Shalom, D. Ressnig, X. Yang, G. Clavel, T. P. Fellingner, M. Antonietti, *J. Mater. Chem. A* **2015**, *3*, 8171–8177.
- [10] X. Jia, Y. Zhao, G. Chen, L. Shang, R. Shi, X. Kang, G. I. Waterhouse, L.-Z. Wu, C. H. Tung, T. Zhang, *Adv. Energy Mater.* **2016**, *6*, 1502585.
- [11] J. Ran, G. Gao, F.-T. Li, T.-Y. Ma, A. Du, S.-Z. Qiao, *Nat. Commun.* **2017**, *8*, 1–10.
- [12] X.-Y. Yang, W. Luo, R. Ahuja, *Nano Energy* **2020**, 104911.

- [13] D. Voiry, R. Fullon, J. Yang, C. d. C. C. e Silva, R. Kappera, I. Bozkurt, D. Kaplan, M. J. Lagos, P. E. Batson, G. Gupta, D. M. Aditya, D. Liang, D. Er, B. S. Vivek, A. Tewodros, C. Manish, *Nat. Mater.* **2016**, *15*, 1003.
- [14] D. Voiry, M. Salehi, R. Silva, T. Fujita, M. Chen, T. Asefa, V. B. Shenoy, G. Eda, M. Chhowalla, *Nano Lett.* **2013**, *13*, 6222–6227.
- [15] H. Li, C. Tsai, A. L. Koh, L. Cai, A. W. Contryman, A. H. Fragapane, J. Zhao, H. S. Han, H. C. Manoharan, F. Abild-Pedersen, J. K. Nørskov, Z. Xiaolin, *Nat. Mater.* **2016**, *15*, 48.
- [16] K. C. Kwon, S. Choi, J. Lee, K. Hong, W. Sohn, D. M. Andoshe, K. S. Choi, Y. Kim, S. Han, S. Y. Kim, H. W. Jang, *J. Mater. Chem. A* **2017**, *5*, 15534–15542.
- [17] A.-Y. Lu, H. Zhu, J. Xiao, C.-P. Chuu, Y. Han, M.-H. Chiu, C.-C. Cheng, C.-W. Yang, K.-H. Wei, Y. Yang, Y. Wang, D. Sokaras, D. Nordlund, P. Yang, D. A. Muller, M. Y. Chou, X. Zhang, L. J. Li, *Nat. Nanotechnol.* **2017**, *12*, 744–749.
- [18] Y. Hao, L.-C. Xu, Z. Yang, R.-P. Liu, X.-Y. Li, J. Pu, L.-F. Huang, *Electrochim. Acta* **2019**, *310*, 153–161.
- [19] J. Zhang, S. Jia, I. Kholmanov, L. Dong, D. Er, W. Chen, H. Guo, Z. Jin, V. B. Shenoy, L. Shi, J. Lou, *ACS Nano* **2017**, *11*, 8192–8198.
- [20] X. Yang, D. Singh, Z. Xu, R. Ahuja, *New J. Chem.* **2020**, *44*, 7932–7940.
- [21] D. Er, H. Ye, N. C. Frey, H. Kumar, J. Lou, V. B. Shenoy, *Nano Lett.* **2018**, *18*, 3943–3949.
- [22] L. Dong, J. Lou, V. B. Shenoy, *ACS Nano* **2017**, *11*, 8242–8248.
- [23] X. Yang, D. Singh, Z. Xu, Z. Wang, R. Ahuja, *J. Mater. Chem. C* **2019**, *7*, 12312–12320.
- [24] H. Yuan, M. S. Bahramy, K. Morimoto, S. Wu, K. Nomura, B.-J. Yang, H. Shimotani, R. Suzuki, M. Toh, C. Kloc, X. Xu, R. Arita, N. Nagaosa, Y. Iwasa, *Nat. Phys.* **2013**, *9*, 563.
- [25] G. Kresse, J. Furthmüller, *Phys. Rev. B* **1996**, *54*, 11169.
- [26] G. Kresse, D. Joubert, *Phys. Rev. B* **1999**, *59*, 1758.
- [27] J. Perdew, K. Burke, M. Ernzerhof, *Phys. Rev. Lett.* **1996**, *77*, 3865–3868.
- [28] J. Heyd, G. E. Scuseria, M. Ernzerhof, *J. Chem. Phys.* **2003**, *118*, 8207–8215.
- [29] A. Svane, O. Gunnarsson, *Phys. Rev. Lett.* **1990**, *65*, 1148.
- [30] H. Monkhorst, J. Pack, *Phys. Rev. B* **1976**, *13*, 5188–5192.
- [31] S. Grimme, J. Antony, S. Ehrlich, H. Krieg, *J. Chem. Phys.* **2010**, *132*, 154104.
- [32] A. Togo, F. Oba, I. Tanaka, *Phys. Rev. B* **2008**, *78*, 134106.
- [33] S. Nosé, *J. Chem. Phys.* **1984**, *81*, 511–519.
- [34] E. Sanville, S. D. Kenny, R. Smith, G. Henkelman, *J. Comput. Chem.* **2007**, *28*, 899–908.
- [35] C. Ataca, H. Ahin, S. Ciraci, *J. Phys. Chem. C* **2012**, *116*, 16, 8983–8999.
- [36] Y. Ding, Y. Wang, J. Ni, L. Shi, S. Shi, W. Tang, *Physica B + C* **2011**, *406*, 2254–2260.
- [37] T. Cheiwchanchamnangij, W. R. Lambrecht, *Phys. Rev. B* **2012**, *85*, 205302.
- [38] X. Ma, X. Wu, H. Wang, Y. Wang, *J. Mater. Chem. A* **2018**, *6*, 2295–2301.
- [39] H. Shi, H. Pan, Y.-W. Zhang, B. I. Yakobson, *Phys. Rev. B* **2013**, *87*, 155304.
- [40] G.-B. Liu, D. Xiao, Y. Yao, X. Xu, W. Yao, *Chem. Soc. Rev.* **2015**, *44*, 2643–2663.
- [41] X. Zhang, X. Zhao, D. Wu, Y. Jing, Z. Zhou, *Nanoscale* **2015**, *7*, 16020–16025.
- [42] M. Gajdoš, K. Hummer, G. Kresse, J. Furthmüller, F. Bechstedt, *Phys. Rev. B* **2006**, *73*, 045112.
- [43] V. A. Medvedev, J. Cox, D. D. Wagman, *CODATA key values for thermodynamics*, Hemisphere Publishing Corporation New York **1989**.
- [44] H. B. Michaelson, *J. Appl. Phys.* **1977**, *48*, 4729–4733.
- [45] G. Henkelman, B. P. Uberuaga, H. Jónsson, *J. Chem. Phys.* **2000**, *113*, 9901–9904.
- [46] A. Kuc, T. Heine, *Chem. Soc. Rev.* **2015**, *44*, 2603–2614.
- [47] A. J. Medford, A. Vojvodic, J. S. Hummelshøj, J. Voss, F. Abild-Pedersen, F. Studt, T. Bligaard, A. Nilsson, J. K. Nørskov, *J. Catal.* **2015**, *328*, 36–42.
- [48] B. Hammer, J. K. Nørskov, *Nature* **1995**, *376*, 238–240.

Manuscript received: March 29, 2020

Revised manuscript received: September 3, 2020

Accepted manuscript online: September 4, 2020

Version of record online: September 28, 2020